Multiphysics Simulations of Representative Hypersonic Vehicle Structures

Eric L. Blades, Parthiv Shah, Michael Nucci, and Scott Miskovish

ATA Engineering, Inc., San Diego, CA 92130

Abstract: This paper extends a previously developed computational framework for coupled aerothermoelastic simulations for hypersonic vehicle structures in extreme environments. An aeroheating verification and validation case is first conducted on a Mach 6.5+ spherical dome protuberance that was tested in a NASA wind tunnel. ATA's simulation includes aerothermoelasticity in the physics and captures the heating of the compliant dome structure during the first five seconds of exposure to hypersonic flow. This case is followed by a coupled quasi-static aerothermoelastic analysis of an acreage panel-level structural component for a sustained, reusable, air-breathing Mach 5–7 cruise horizontal-takeoff platform. The panels were consistent with the NHV outer mold line (OML), allowing the fully coupled simulation of two realistic structures in a realistic hypersonic environment. The paper presents results from a first quasi-static simulation of an orthogrid stiffened, curved panel that bows into the flow due to thermal stress and an assumed internal pressure. The effect of the stiffeners on the panel's response is profound and includes global and localized bowing relative to the undeformed panel and vehicle OML, resulting in the generation of multiple shock structures.

1. Introduction

United States Air Force (USAF) reusable sustained hypersonic cruise vehicle designs will require durable structures capable of extended-duration operations in combined, extreme environments, typified by significant thermal, acoustic, and mechanical loading with large spatial and temporal gradients and nonlinear, coupled interactions between the structure and the environment. To support the USAFọs overarching objectives, ATA Engineering, Inc., (ATA) is conducting detailed coupled quasi-static and dynamic aerothermoelastic analysis of acreage panel-level single or multiple-bay structural components for a sustained, reusable, air-breathing, Mach 5ï 7 cruise horizontal-takeoff platform. The current effort builds on ATAọs previous program to develop a multiphysics coupled analysis capability for hypersonic vehicle structures (Blades 2011, 2011). Panels are being provided by the Structural Sciences Center (SSC) of the Air Force Research Labọs (AFRLọs) Air Vehicles Directorate as part of their current structural design, development, and validation studies, which include both industry and internal research efforts.

2. Objectives

The objective of the present work is to conduct both quasi-static and dynamic analysis of a notional hypersonic flight panel design developed by industry in a parallel development effort supported by AFRL.

It is anticipated that this effort will uncover, better define, and document shortcomings in the methods used currently by the aerospace industry to analyze and predict the life of extreme environment hot structures. ATA is using a two-stage analysis procedure that includes:

(1) Quasi-static analysis at the level of a full three-dimensional hypersonic vehicleôs aerothermal flowfield (i.e., the entire vehicle or a sufficient volume encompassing the panel and locally wetted vehicle substructure) at a specific flight condition (i.e., point in trajectory) to define global thermal and quasi-static pressure loads, where only regions local to the panel will be considered to be compliant.

(2) Unsteady coupled aerothermoelastic analysis of a local panel region on the hypersonic vehicle (time-accurate for bandwidth up to 200 Hz), using unsteady load perturbation from the quasi-static full-vehicle analysis in (1) above.

3. Technical Approach

In a domain-decomposition approach to a coupled aero-thermal-structure interaction problem, the CFD code will compute the traction (or pressure) vector and the heat flux at the fluid-structure interface (or wetted surface), and the NLCSD code will compute the resulting temperatures and structural displacements due to those loads. The overall procedure for a typical problem is illustrated in Figure 1 and is as follows when the CFD code leads:

1. Obtain the CFD solution for the boundary conditions at time level, n, and compute
   a. the traction vector, $\vec{T}_w^{(f,n)}$, acting at the boundary faces on the fluid interface, *f*, and
   b. the concentrated heat flux, $H_w^{(f,n)}$, (an integrated, area-weighted nodal value) acting on the fluid interface.
2. Map the fluid domain solution quantities to the structural domain.

a. Map the elemental traction vector, $\vec{T}_w^{(f,n)}$, from the boundary faces of the fluid interface to a nodal force vector, $\vec{F}_w^{(s,n)}$, at the nodes of the solid interface, s, in a conservative manner.

b. Map the concentrated heat flux, $H_w^{(s,n)}$, from the nodes of the fluid interface to the nodes of the solid interface.

3. Obtain the NLCSD solution to compute the displacements of the elastic body.

4. Map the structural domain solution quantities to the fluid domain.

a. Map the displacements, $\vec{x}_w^{(s,n+1)}$, from the nodes of the solid interface to the nodes of the fluid interface, $\vec{x}_w^{(f,n+1)}$, in a conservative manner.

b. Map the temperature, $t_w^{(s,n+1)}$, from the nodes of the solid interface to the nodes of the fluid interface, $t_w^{(f,n+1)}$.

5. Move the interior CFD computational domain to reflect the structural deformation (i.e., volume grid adaptation).

6. Repeat for time level *n+1*.

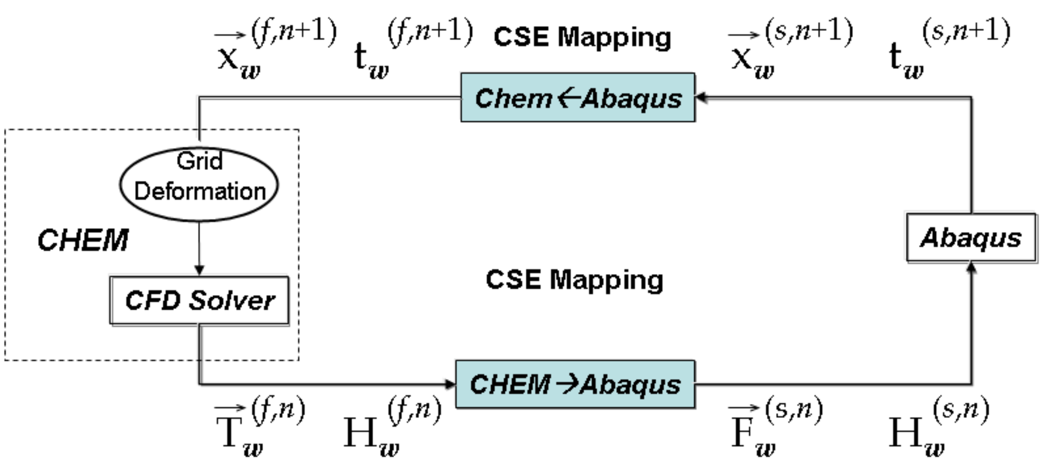

Figure 1. Multiphysics co-simulation procedure.

Since a domain-decomposition approach is utilized, each domain will be suitably discretized for the appropriate solver. As such, the interface between the two domains will almost certainly be discretized differently and will not match. The data transfer at the wetted surface interface is done using the mapping tools provided by the CSE. Once the CFD wetted surface is moved to conform to the structural deformations, the flow solver adapts the volume grid to reflect these changes (Luke, 2012).

The Loci/CHEM CFD solver was used to compute the solution for the fluid domain. Loci/CHEM is a Reynolds-averaged Navier-Stokes finite-volume flow solver for arbitrary polyhedra developed by Dr. Edward Luke at Mississippi State University (MSU) (Luke, 2005, 2007). CHEM uses density-based algorithms and employs high-resolution approximate Riemann solvers to solve finite-rate, chemically reacting viscous turbulent flows. The coupling between the CHEM and Abaqus is accomplished using SIMULIA's Co-Simulation Engine (CSE).

4. Hypersonic Fluid-Thermal Validation Case

Because of the extreme nature of hypersonic environments and difficulty to conduct experiments at these conditions, it is desirable perform multiphysics simulations to replicate these conditions. However, this difficulty of experimentally replicating these environments has resulted in a limited data available for validation of such simulations. The validation data case presented here is for a hypersonic fluid-thermal experiment. A series of hypersonic wind tunnel experiments were conducted at the NASA Langley 8-Foot High Temperature Tunnel (HTT) to investigate the thermal effects of deformed thermal protection system panels (Glass 1986, 1988). The experiments inserted a series of rigid, dome-shaped protuberances into a hypersonic flow and measured the thermal and structural loads on the protuberances. The tested configurations consisted of single a protuberance, a span-wise row of protuberances, and a quilted array of protuberances. The protuberances represented the structural deformations of the thermally bowed panels due to through-thickness thermal gradients in the panels.

The HTT is a blowdown tunnel capable of simulating aerodynamic heating and pressure loading for a nominal Mach 7 flow at altitudes between 80,000 and 120,000 feet. The energy needed for these hypersonic flows comes from burning a mixture of air and methane under pressure in the combustion chamber and expanding the products through a nozzle into the test chamber. Due to the combustion process, the freestream properties in the test chamber are based on the equivalence ratio of the fuel to oxidizer in the combustor. The equivalence ratio is given as $\phi = \frac{(m_{fuel}/m_{ox})_{actual}}{(m_{fuel}/m_{ox})_{stoichiometric}}$. However, the equivalence ratios in the combustor were not provided in the test report. Fortunately, Ostoich (Ostoich 2011, 2012) performed a series of numerical experiments as part of their validation studies to estimate the flow conditions and found that an equivalence ratio of 0.7 most closely matched the freestream conditions reported in the hypersonic experiments. Using this value for the equivalence ratio, the values for the fluid transport properties and specific heat were digitized from the charts for methane-air mixtures (Leyhe, 1962) and used for the simulations presented here.

In the hypersonic flow experiments, the test article, which consisted of the panel and protuberance configuration, was inserted into the flow at a 5° angle of attack. The experimental configuration is shown in Figure 2. The experiments were conducted under both laminar and turbulent boundary-layers and the results presented here are for laminar conditions. The laminar boundary-layer over the inclined panel was generated by a blunt 3/8ò leading edge radius. The laminar state of the flat plate (no protuberance) boundary-layer was verified by comparison of the measured and predicted boundary-layer profiles as shown in Figure 3.The run conditions are listed in Table 1. An isothermal boundary condition of 300K was applied to the panel.

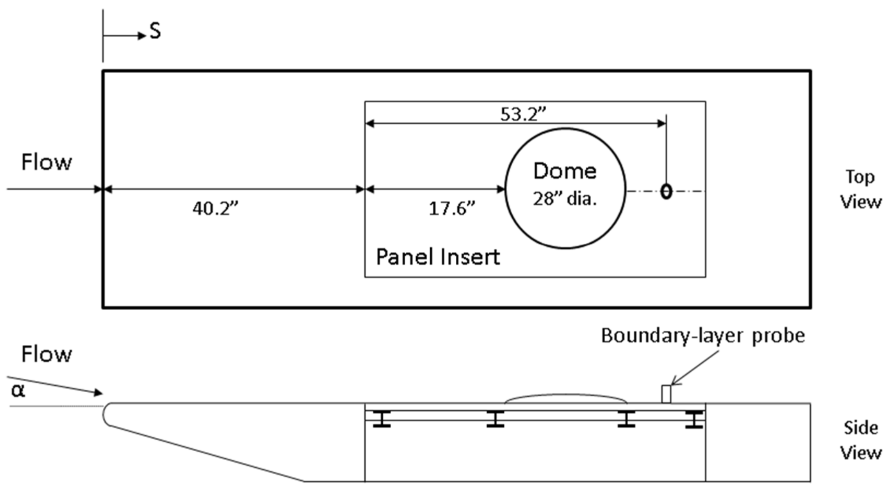

Figure 2. Schematic diagram of panel holder and dome model.

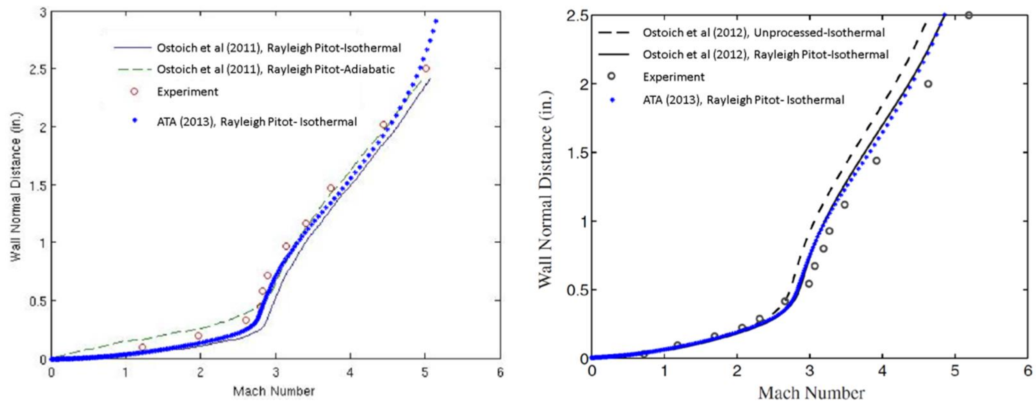

(a) (b)

Figure 3. Boundary-layer profile comparison at (a) x=26.2” and (b) x=58.1” downstream of the leading edge.

Table 1. Freestream conditions for Glass and Hunt validation cases

Experimental Run No.	Mach Number	$P_{Ð}$, psia	$T_{Ð}$, °R	BL Probe Location, in
1 (Glass, 1986)	6.55	0.095	419	58.1
1 (Glass, 1988)	6.53	0.096	419	26.2
14 (Glass, 1986)	6.59	0.094	420	N/A

For the first run in both the 1986 and 1988 series of experiments, the dome was replaced by a flat disk and the boundary layer was measured using a probe to verify that the experimental set was generating a laminar boundary layer. These experimentally measured boundary-layer profiles were used for comparison to provide confidence in the value of the equivalence ratio used in the numerical simulations. A two-dimensional CFD simulation was performed using the gas properties corresponding to an equivalence ratio of 0.7 (Leyhe, 1962) to verify the boundary-layer profile. The domain for the two-dimensional CFD simulations is shown in Figure 4. A viscous grid was generated using an initial normal spacing that resulted in y+ values of less than 0.1 on the surface of the dome. A boundary-layer growth ratio of 3 percent was used and resulted in 158,395 hexahedral cells in the domain. A uniform inflow boundary condition consistent with the experimental run conditions listed in Table 1 was specified for the inflow and far field (top boundaries), a supersonic outflow boundary condition was applied to the outflow boundary, and an isothermal boundary condition of 300 K was applied to the panel. A comparison of the measured and predicted boundary-layer profiles is shown in Figure 3. Overall, the results compare well with the experimental profiles and with the past analytical results (Ostoich, 2011, 2012).

The experimental values (Glass, 1986) were derived from measurements taken using a boundary-layer probe. A supersonic boundary-layer probe is an invasive measurement. Its presence causes a local bow shock such that the stagnation pressure measured by the pitot tube is the same as that associated with the post-shock flow. The experimental values shown in Figure 3 are pre-shock measurements computed using the Rayleigh pitot tube formula given by the following equation:

$$\frac{p_{t2}}{p_{fp}} = \left(\frac{(\gamma+1)^2 M_1^2}{4\gamma M_1^2 - 2(\gamma-1)} \right)^{\frac{\gamma}{\gamma-1}} \frac{(1-\gamma) + 2\gamma M_1^2}{\gamma+1} .$$

This equation relates the total pressure after the shock (pt2) to the static pressure before the shock (pfp). The values from the numerical simulations were computed in a similar manner using a local value for gamma. A comparison of the measured and predicted boundary-layer profiles is shown in Figure 3. For reference, the results from similar simulations performed (Ostoich, 2011, 2012) are also included in Figure 3. Overall, the results compare well with the experimental profiles and with the results from these references.

Run 14 from the 1986 experiment was selected as the validation case. This run features a single aluminum dome installed in a ceramic flat plate. The spherical dome has a protuberance diameter of 28 inches and a height of 0.76 inches. The backside of the dome is exposed to an evacuated chamber. The dome is made from 14 gauge aluminum sheet metal, and the plate is made from Resco Cast RS-17E refractory ceramic. The thermal and mechanical properties for the two materials are shown in Table 2, with mechanical properties for the ceramic material based on estimates for other aluminum silicate materials.

In an effort to reduce computational expense, the domain of the coupled, three-dimensional aerothermoelastic simulation does not extend all the way to the blunt leading edge of the plate. Rather, the domain begins 40.8 inches downstream of the leading edge, and the boundary-layer profile and flow conditions from the two-dimensional simulation at this station were specified as the inflow conditions for the fluid domain. The white outline shown in Figure 4 illustrates the extent of the three-dimensional fluid domain. Similar boundary-layer spacing parameters used to create the 2-D grid were also used to create the three-dimensional fluid mesh and resulted in 7,479,658 hexahedral cells. The surface mesh for the fluid domain is shown in Figure 6; note that the wetted surface interfaces between the fluid and structural domains are not point-matched, as the fluid-domain wetted interface is considerably more refined than the structural domain. Far-field boundary conditions were applied to the top boundary surface, symmetry conditions were applied to the sides of the domain, and supersonic outflow boundary conditions were applied to the outflow surface.

The structural model is shown in Figure 5, including a zoomed-in view of the discretization through the thickness of the domain. The aluminum dome was meshed using eight-node solid elements with ten elements through the thickness. The ceramic plate uses the same mesh density near the surface to capture the thermal gradients at the wetted surface interface, and the mesh size increases as it moves deeper through the plate. The structural domain contains 47,289 nodes and 42,760 elements. The mechanical boundary conditions consisted of appropriate symmetry conditions along each side of the domain, and the normal displacement (y-direction) was restrained on the bottom of the plate. The thermal boundary conditions are set to adiabatic everywhere except for the co-simulation surface. The initial condition in the structural domain is a uniform temperature of 300 K.

Table 2. Thermal and mechanical material properties for the Glass and Hunt case

Material	Density (kg/m^3)	Conductivity (W / m·K)	Specific Heat (J / kg·K)	Coefficient of Thermal Expansion	Youngŝ Modulus (MPa)	Poissonŝ Ration
Resco RS-17E	2192	1.07	750	12.3e-6	70	0.22
Aluminum	2800	155.0	883	23.2e-6	72	0.33

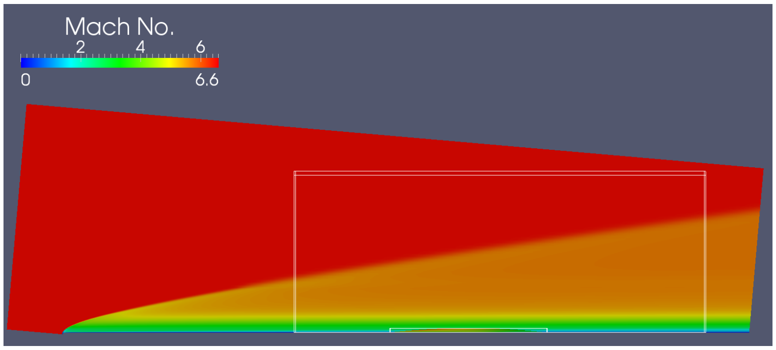

Figure 4. Two-dimensional fluid domain and extent of the three-dimensional domain (white outline) for the Glass and Hunt validation case.

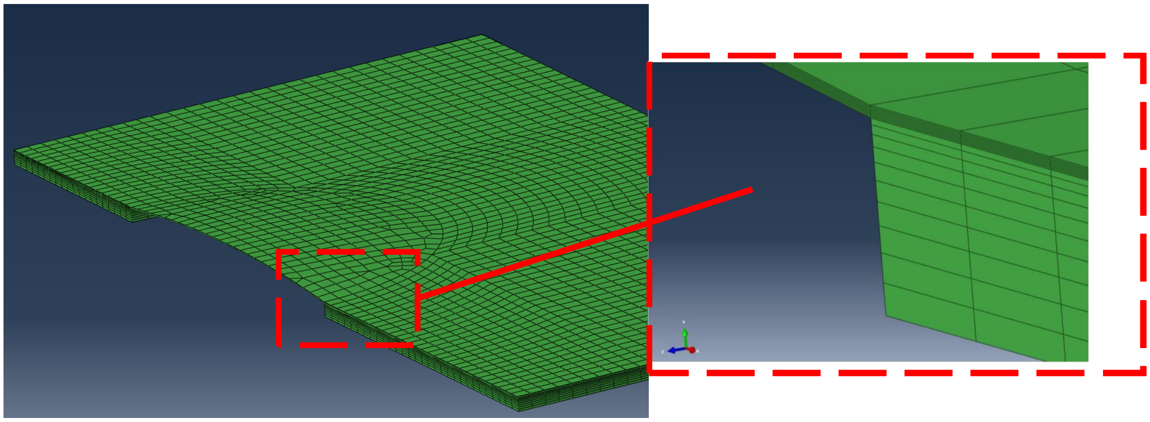

Figure 5. Structural domain showing surface mesh and zoomed-in view of through-thickness mesh

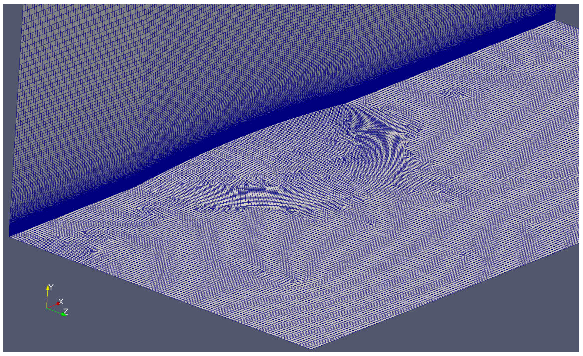

Figure 6. Fluid domain for the Glass and Hunt validation case.

Transient aerothermoelastic co-simulations were run for the panel assembly inserted into a Mach 6.59 freestream corresponding to the 1986 Run 14 conditions. For these types of simulations involving hypersonic flows, the ratio of time scales between the pertinent structural and fluid physics are on the order of O(103). Because of the disparate time scales between the structural and fluid domains, the temporal coupling is done in a quasi-static manner. Recall that the goal of the experiments and thus the current work is to determine the transient thermal response of a structure in the hypersonic environment with a laminar boundary layer; thus it is not necessary to resolve the small time scales in the fluid solution. Following the approach of previous work (Ostoich, 2011, 2012), the time-accurate solution for the structural domain at the $n + 1$ time step is found by integrating the solution given the mechanical load and heat flux provided by the fluid solution at time step n. The interface temperature is given as a boundary condition in the fluid domain, and the fluid is marched from time step n to the steady-state solution consistent with the $n + 1$ interface temperature. A convergence study was performed over the initial 0.1 seconds, and it was found that 200 fluid iterations using local time stepping were sufficient to achieve a steady-state fluid solution. Thus, time-accurate simulations were run for 5 seconds using a time step of 0.01 seconds for the structural domain, and the fluid domain performed 200 steady-state iterations for every structural time step.

The first quantitative comparison made was the instantaneous heat flux into the panel at a short time after insertion. The exact time was not specified in the Glass and Hunt reports other than as ña short time after insertion, but for comparison to past work, the heat flux was computed at 0.1 seconds (Ostoich, 2011). Glass and Hunt estimated the local heat flux, q, using the equation $q = \rho C_p \tau (\Delta T/\Delta t)$ under the assumption of one-dimensional heating under perfectly insulated conditions on the back side of the dome and constant through-thickness. They constructed a central differenced approximation to the rate of temperature increase, $\Delta T/\Delta t$, and combined this with the dome properties (density, ρ, thickness, τ, and specific heat, C_p) to come up with a heat flux value. As shown in Table 3, the results compare well with previous works (Ostoich, 2011), though the two computational approaches may lead to modest differences (aerothermoelastic vs. aerothermal only). Also worth noting is that the largest discrepancy from the experiment occurs at the same sensor locations on the periphery of the dome model (see red circles in Figure 7). In the current analysis, the temperature-time histories are taken from the nearest cell center of the CFD solution, interpolated from the structural domain, so that may explain some discrepancy.

Additionally, the heat-flux estimator assumes no net in-plane heat transfer, which may become more important at the periphery of the dome panel.

Table 3. Computed heat fluxes compared to experiment and Ostoich et al.'s computations

Thermo-couple	Current Result % Diff	Ref **Error! Reference source not found.** (aerothermal only) % Diff
2	ï 11.933	ï 7.19
3	1.309	ï 0.91
4	1.447	+7.47
7	2.040	+11.86
10	3.734	+11.01
12	ï 25.290	ï 19.40
19	ï 7.841	ï 1.74
21	ï 25.494	ï 18.96
28	ï 3.587	+2.33
30	ï 16.697	ï 5.29
37	ï 6.171	+1.26
39	ï 9.399	+1.54
41	ï 4.340	+4.51

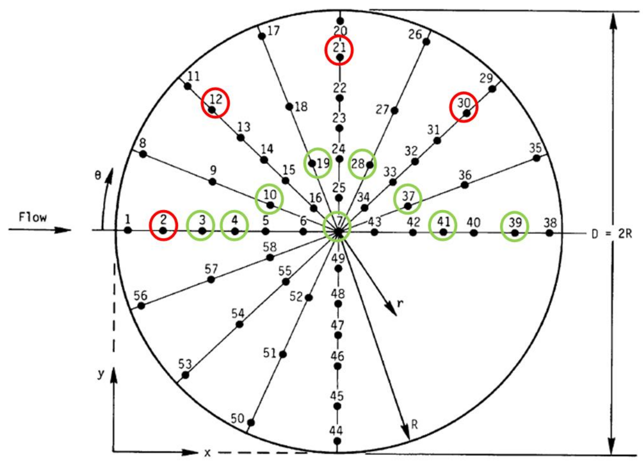

Figure 7. Selected probe locations for heat flux reporting at 0.1 seconds into simulation

Figure 8 presents CFD solution contours on the dome panel and tunnel wall surface and on the symmetry plane at one second into the simulation. The spherical shape of the dome generates a local shock structure that can be seen in both the Mach number and temperature contours. The flow creates an upstream compression and downstream expansion that result in higher pressure and heat fluxes on the forward portion of the dome. Evidence of secondary flow in the form of a horseshoe vortex is also seen in the surface heat transfer contours plot as a streak on the side of the dome.

Figure 9 presents surface temperatures at 1, 3, and 5 seconds into the aerothermoelastic co-simulation. The peak deflection at 5 seconds is 1.5 mm and occurs at the center of the panel. In general, the results are comparable to previous works, suggesting that during the first 5 seconds, the elasticity of the dome panel is not critical to the heat flux estimation (Ostoich, 2012). It should be noted, however, that the dome deformation of 1.5 mm at 5 seconds is not trivial, as shown in the time evolution of the coupled temperature-displacement modelôs through-thickness temperature on the symmetry plane of Figure 10. Note that the images in the figure have been anisotropically scaled in the vertical direction by a factor of 3 to better show the through-thickness temperature. The figure validates the assumption of no through-thickness temperature gradient used in the heat flux estimation (comparison to experiment) at 0.1 seconds. While not critical at 5 seconds, the inclusion of an elastic component to the co-simulation was acknowledged as a possible means to improve accuracy over longer time scales (e.g., 50 seconds) when the deflections are more significant and will have a greater impact on the local surface pressure and heating rates (Ostoich, 2012).

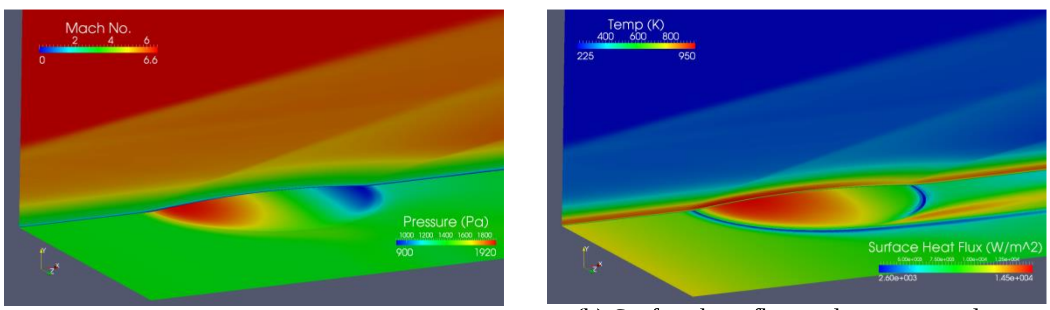

(a) Surface pressure and symmetry plane Mach number

(b) Surface heat flux and symmetry plane temperature

Figure 8. CFD solution contours at time t = 1 seconds

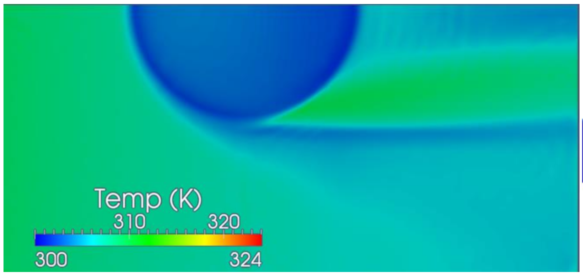

(a) t = 1 s

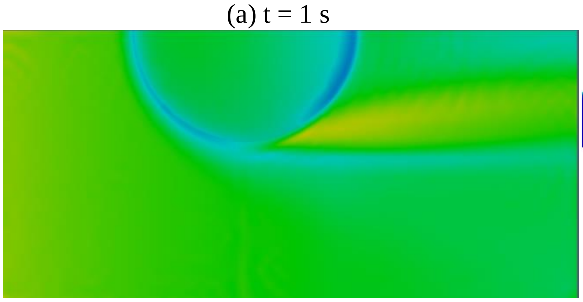

(b) t = 3 s

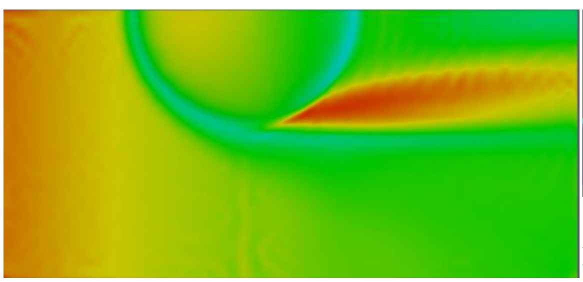

(c) t = 5 s

Figure 9. Top-down view of surface temperature evolution during first five seconds

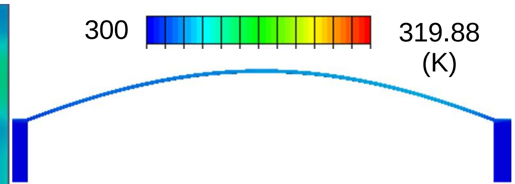

(a) t = 1 s

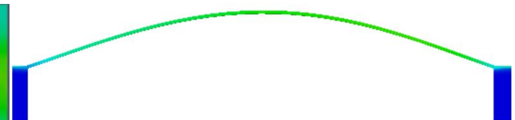

(b) t = 3 s

(c) t = 5 s

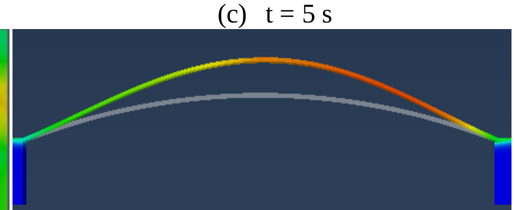

(d) Same as (b) with pressure contours

Figure 10. Side view of temperature through FEM during first five seconds. Vertical scale stretched by 3:1 to better illustrate through-thickness temperature and aerothermoelastic deformation

The aerothermoelastic validation of the Glass and Hunt case demonstrates that the computational framework and analysis methods are suitable to a coupled modeling of a realistic flight panel in a similar hypersonic regime. This is discussed in the next section.

5. Hypersonic Flight Panel Simulation

A hypersonic flight panel simulation was performed to demonstrate the capability of the analysis method on realistic structure subjected to a realistic incoming hypersonic flowfield, including boundary layer. Two panels were defined to have wetted surfaces coincident with different portions of the vehicle. As shown in Figure 11, ATA developed a notional hypersonic vehicle (NHV) geometry by combining its previous forebody (Blades, 2011) with a representative aftbody definition. In general, the ATA vehicleôs outer mold line (OML) was designed to be smooth and included a delta wing and a single vertical tail similar to the notional vehicle found in the literature (Zuchowski, 2012). The overall length of the vehicle was 31.3 m (102.5 ft), with a wingspan of 11.2 m (36.6 ft). No propulsion system was modeled on the underside of the vehicle since the two panels of interest were on the upper vehicle surface.

A panel with modest curvature was located on the upper side of the vehicle about 18.2 m (59.7 ft) from the nose, and a second panel with significant curvature was located near the aft of the upper side of the vehicle about 26.5 m (86.9 ft) from the nose. The goal of the vehicle OML definition was to provide a reasonably realistic flow environment for the purposes of coupled analysis, but it was not intended to satisfy any aerodynamic design or performance objective. The panel definitions were based on the notional Boeing and Lockheed Martin panels shown in their respective contractor reports. Because the actual panels were not exactly coincident with ATAôs NHV, these panel models were adapted to the NHV OML; therefore, direct comparison between the studies is not possible. In general, the results shown here represent more of a demonstration of the ability to perform such coupled analyses using realistic geometries and vehicle definition rather than a coupled analysis to complement the previous industry analyses that are based on superposition of various load cases such as thermal loading, maneuvering, acoustics, etc. To perform the latter requires a close coordination of a multidisciplinary team from the onset of the program to ensure that the assumptions made to each individual analysis may be reconciled for a meaningful co-simulation.

A single cruise condition of Mach 5.2, 71,500 ft, was selected as the operating condition (Zuchowski, 2012). The Reynolds number based on vehicle length was above 2x108, so the Reynolds-Averaged Navier-Stokes equations were selected for the CFD module using the Menterôs SST turbulence model. Radiative equilibrium to 0 K was modeled as the surface temperature boundary condition over the entire vehicle, and the aircraft angle of attack was kept at 0 degrees for the case shown in the present study.

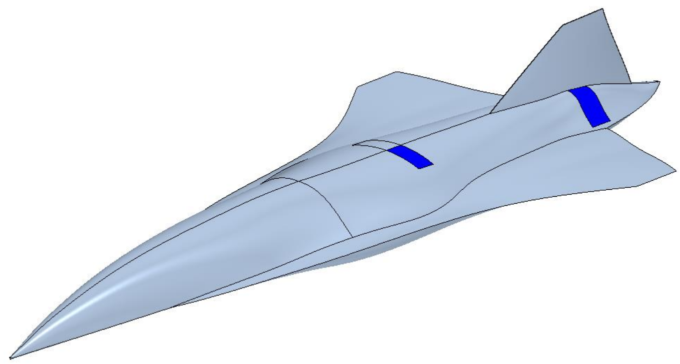

Figure 11. ATA NHV showing panels 1 (forward) and 2 (aft) in dark blue.

Rigid CFD was first run as a half-symmetry model. The surface was finely meshed with additional resolution at the two panel locations to allow subdomains to be easily extracted for co-simulation. The total vehicle solution mesh had 26 million cells, with y+ less than 0.5 everywhere on the vehicle. The mesh consisted of prismatic volumes in the near-wall region and unstructured tetrahedral volumes elsewhere. Figure 12 presents the rigid CFD solution, showing the radiative equilibrium temperature on the vehicle surface and the Mach number on the symmetry plane. In general, the surface temperature in the undeformed regions of panels 1 and 2 is found to be around 750 K on this vehicle.

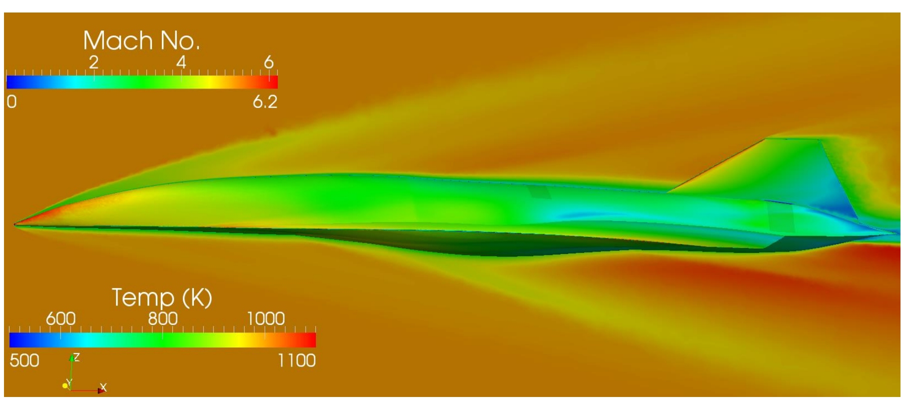

Figure 12. Rigid CFD solution on ATA NHV at Mach 5.2, 71,500 ft. Radiative equilibrium temperature shown on vehicle surface and Mach number shown on symmetry plane. Panels 1 and 2 darkened for emphasis.

5.1 Structural Models

Panel 1 was nominally based on the orthogrid design of Panel 862 by Boeing, Research and Technology (Quiroz, 2012). ATAǿs model consists of 9,812 nodes and 10,125 elements and is pictured in Figure 14. Similar to Boeingǿs Panel 862 design, the panel is an orthogrid stiffened panel utilizing a 0.762 m x 0.762 m (3 inch x 3 inch) stiffener spacing; it has eighteen stiffeners on its longer side and ten stiffeners on its shorter side. ATA projected the notionally flat 1.355 m x 0.701 m panel described by Boeing to fit on the curved upper surface of the NHV, thereby fundamentally altering its stiffness. The shorter panel dimension was roughly oriented with the flow, while the longer dimension was roughly spanwise.

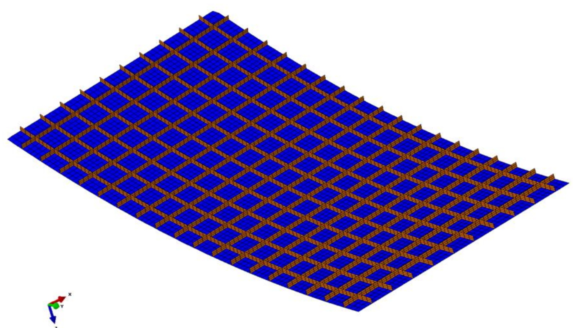

Figure 13. Curved panel finite element model.

5.2 Computational Fluid Dynamics Models

To reduce the computational expense, a subdomain model for the volume surrounding the panel was extracted directly from the original volume mesh. The extracted subdomain mesh contained 4.56M cells. Boundary conditions data was extracted from the rigid CFD solution in the spherical region around the panel, as shown in Figure 14. The radius of the spherical region was approximately three panel lengths. Extracted data included all CFD variables required to simulate the local flow around the panel and thereby reduce the overall size of the co-simulation domain.

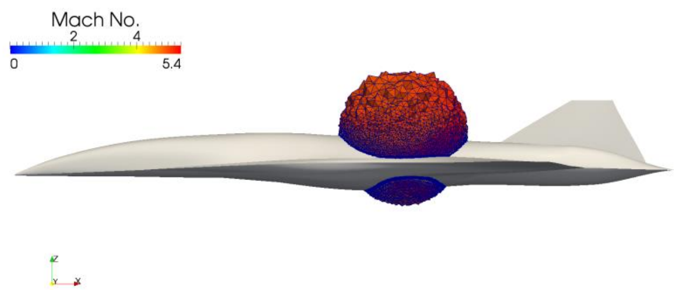

Figure 14. Point cloud data from full CFD simulation, colored by Mach number.

5.3 Multiphysics Simulations

The CFD solution was run as a co-simulation in a steady-state mode to achieve a deformed quasi-steady panel shape. The structural model was solved in Abaqus/Standard using the implicit ñcoupled-temperature displacementò solver. Radiative equilibrium from the panel was handled by Abaqus, so the CFD code could pass heat fluxes and Abaqus would return surface temperatures. The CFD code was allowed to subcycle, and the information exchange between the two domains occurred every fifth fluid iteration. The panel boundary conditions were pinned for simplicity, and an internal pressure of 13789.5 Pa (2 psi) was applied to simulate a pressurized compartment. Again, these loads and pinned boundary conditions were not intended to capture the true time-dependent state of growth of the panel relative to the vehicle but were used for the purpose of demonstration, and they represent an extreme-environments example of high thermally induced stress relative to a more compliant substructure.

The converged Abaqus solution is shown in Figure 15. In the left figure, the deformed curved panel is shown to scale, while in the right figure, the deformation relative the curved unloaded geometry is exaggerated by a factor of 10. Due to the vehicle curvature and the flowfield nonuniformity, the panel does not deform with bidirectional symmetry as would the first mode of a flat panel under uniform loading. The maximum displacement is about 3.2 cm, or just less than 5% of the panel length in the streamwise direction, and occurs closer to the vehicle symmetry plane. The Abaqus solution indicates that in addition to the large-scale deformation there is also bowing (principally outward) of the skin on individual orthogrid cells, revealing an ñegg-crateò pattern when the deformation is exaggerated.

Figure 16 presents the converged solution from the CFD solver. In the left figure, the surface temperature is shown on the vehicle surface, revealing regions of elevated temperature on the forward side of the deformed panel followed by regions of reduced temperatures on the aft side. The Mach number contours in the left figure are shown on a constant spanwise plane that cuts through the hottest orthogrid cell on the panel leading edge, about 42% of the spanwise panel length from the rigid vehicleĝs symmetry plane. This reveals a shock structure that is created by the panelĝs leading edge deformation. The pressure plots on the right indicate regions of high and low pressure relative to local values in the flow (away from the panel) that are caused by the deformation into the flow. Temperature and pressure contours reveal that the local deformations seen in Figure 15 are correlated to local changes in the flowfield.

An alternate view of the flowfield due to the deformed panel is shown in Figure 17. As viewed from the other side of the vehicle, it is clear that at the leading edge there are certain orthogrid cells that do not heat up as much as their neighbors on the leading edge. In some cases, inward bowing was seen on the corners. It is not clear whether this is a result of the somewhat unrealistic simple pinned boundary conditions. The figure reveals that the shock is actually detached upstream of the panel leading edge, as seen by the shock line and the location of rapid growth of the thermal boundary layer, but there is a local deviation from this feature at the symmetry plane where the corner orthogrid cell appears to have bowed inward and local expansion inhibits the formation of a shock. Shear stress contours on the right figure also suggest that there can be some secondary flows generated in these cells. Figure 18 uses an enhanced color scale to show pressure contours on the vehicle surface and symmetry plane. The additional contrast clearly reveals localized individual shocks forming on each orthogrid panel and in some cases coalescing at some distance above the vehicle surface.

Figure 19 plots the normalized convergence history of the three components of force and the integrated heat load on the panel. The plot clearly demonstrates that the co-simulations have converged, though there occasionally appear to be impulsive spikes in the heat load, especially early during convergence. Monitoring of select nodes at the leading edge suggests some locally isolated but erratic temperature history that is hypothesized to occur because the radiative equilibrium boundary condition is being handled by two different codes. This fluctuation in local behavior may also improve if the pinned boundary conditions are relaxed to simulate an equivalent compliant substructure. This is a topic of ongoing work. Taken *in toto*, the converged quasi-static aerothermoelastic simulation of the stiffened panel under a realistic hypersonic flowfield suggests that the coupled multiphysics can provide additional insight into failure mechanisms and a more realistic understanding of design margins than simple uncoupled analyses where CFD is done in a rigid manner to pass loads to CSD tools in a one-way coupling only.

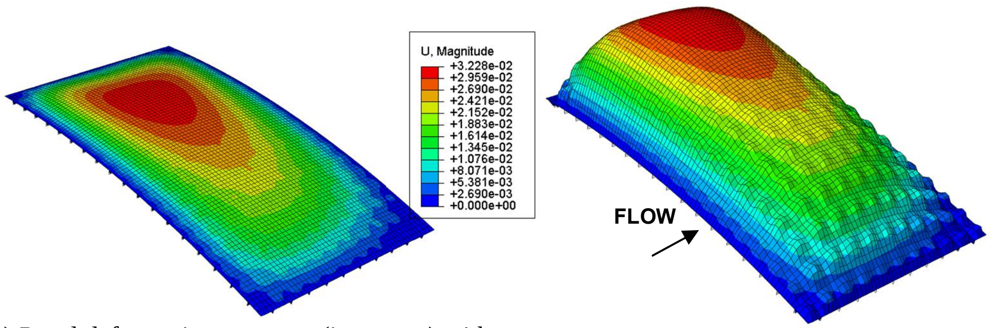

(a) Panel deformation contours (in meters) with actual deformation applied to mesh.

(b) Panel deformation contours with 10x deformation applied to mesh.

Figure 15. Panel deformation.

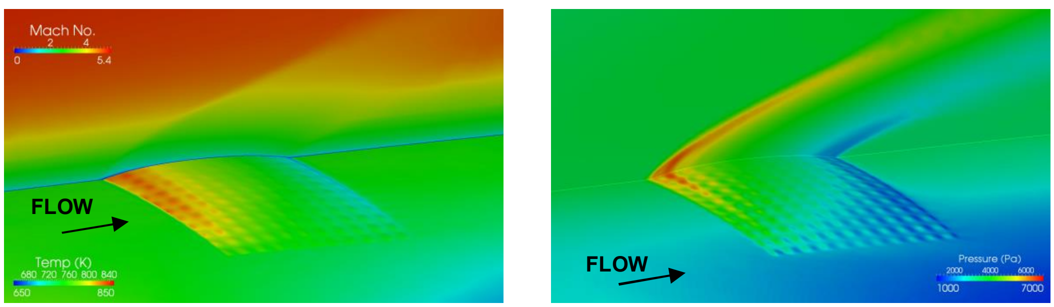

(a) Contours of vehicle and panel surface temperature and Mach number at 42-percent-panel-span cutting plane.

(b) Contours of surface and 42-percent-panel-span cutting plane static pressure.

Figure 16. CFD solution over panel with pinned boundary conditions. Flow from left to right

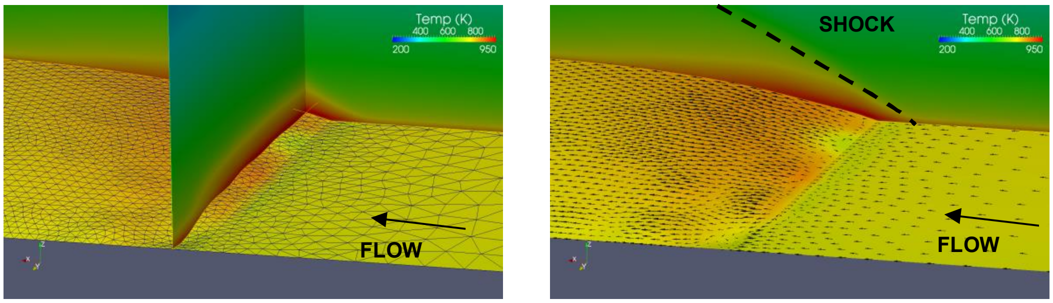

(a) Surface temperature on vehicle surface, 42-percent-panel-span cutting plane, and streamwise cutting plane.

(b) Same as (a) with streamwise plane removed and shear stress vectors shown in vehicle surface plane.

Figure 17. CFD solution over panel with pinned boundary conditions, viewed from vehicle starboard side. Flow from right to left

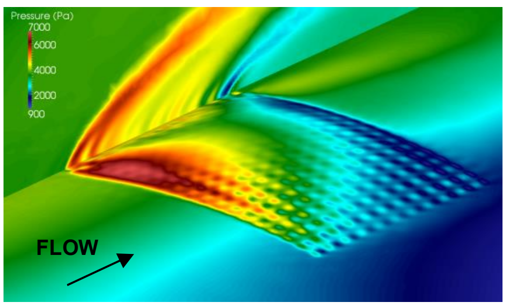

Figure 18. Static pressure on surface and vehicle symmetry plane. Enhanced color scale emphasizes local shock formation due to individual orthogrid deformation

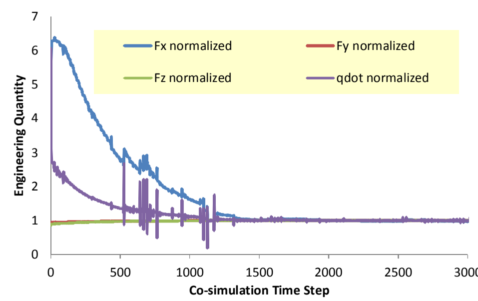

Figure 19. Convergence history of normalized panel forces and heat load

6. Conclusions

Two computational aerothermoelastic studies have been performed in the Mach 5ï 7 flow regime using the Co-Simulation Engine to create a coupled CFD/CSD framework. An aerothermoelastic validation and verification simulation on a Mach 6.5+ protuberance that was tested in NASAôs High Temperature Tunnel demonstrates the ability of the current tools to accurately model the heat transfer in the hypersonic boundary layer. The results show good comparison to computed heat flux data from the original NASA study, as well as good comparison to previous validation studies (Ostoich, 2011, 2012). Because the current simulation included the aeroelasticity of the dome, the result is expected to be useful over longer times where deformations may grow to levels where a significant coupled fluid-thermal-structural interaction occurs.

The second study was for a quasi-static panel-level aerothermoelastic analysis over ATAõs NHV. This curved stiffened panel revealed that, under an appropriate set of boundary conditions and external flow, there is a strong coupling that requires multiphysics analysis to improve accuracy and avoid unnecessary conservatism due to superposition of loads. Additionally, the local subdomain approach used in the analysis framework is a powerful means to quickly and efficiently reduce problem size without having to reinterpolate boundary conditions from the full rigid vehicle CFD domain. Finally, the results shown in the current work represent a demonstration, so no comparison to previous results generated by industry is suggested.

There are several lessons learned that may be applied to the future incorporation of such analysis techniques into the design and analysis process. In the future, if engineering organizations are to perform such multiphysics analyses, it is recommended that communication between disciplines begin early to address some of the differences between modeling assumptions made by fluid, thermal, and structural analysts. For example, the abstraction to mid-surface shell models by thermal and structural analysts must be planned for when communication to a wetted CFD surface is required in co-simulation. Additionally, effort must be expended to properly account for thermal growth and appropriate boundary conditions in the vehicle substructure if a local panel analysis is to be peformed. Finally, the use of a local CFD subdomain is found to greatly speed up computational effort, which is particularly important for dynamic, time-accurate simulations of panel response.

7. Acknowledgements

This work was completed with SBIR funding from Wright-Patterson AFB, contract FA8650-09-M-3930, Dr. S. Michael Spottswood, Program Manager. These simulations these results were obtained in part through the use of computing facilities at the U.S. Army Engineer Research and Development Center DoD Supercomputing Resource Center. The authors wish to thank their ATA Engineering colleagues Mr. Greg Mathy for his computer-aided-design modeling of the NHV geometry and Mr. Azariah Cornish for generating the computational models used in the validation simulations. Special thanks go to Dr. Christopher Ostoich and Prof. Daniel Bodony for helpful discussions related to the Glass and Hunt validation case, and to Dr. George Tzong of Boeing

Research and Technology and Mr. Brian Zuchowski of Lockheed Martin for helpful discussions related to industry panels.

8. References

1. Blades, E. L., R. S. Miskovish, M. Nucci, P. Shah, P. G. Bremner, and E. A. Luke, "Towards a Coupled Multiphysics Analysis Capability for Hypersonic Vehicle Structures," AIAA-2011-1962, 2011.

2. E. Blades, S. Miskovish, E. Luke , E. Collins, and A. Kurkchubashe, "Multiphysics Simulation Capability using the SIMULIA Co-Simulation Engine," AIAA-2011-3397, 2011.

3. Ligoure, S., and G. Tzong, ñIdentification of Knowledge Gaps in the Predictive Capability for Response and Life Prediction of Hypersonic Vehicle Structures,ò AIAA-2011-1961, 2011.

4. Luke, E., E. Collins, and E. Blades, ñA Fast Mesh Deformation Method Using Explicit Interpolation,ò *Journal of Computational Physics*, vol. 231, no. 2, (2012): 586ï 601.

5. Luke, E., and T. George, ñLoci: A Rule-Based Framework for Parallel Multidisciplinary Simulation Synthesis,ò *Journal of Functional Programming* (Cambridge University Press) vol. 15, no. 3 (2005): 477ï 502.

6. Luke, E., ñOn Robust and Accurate Arbitrary Polytope CFD Solvers (Invited),ò AIAA 2007-3956, 2007.

7. Glass, C. E., and R. L. Hunt "Aerothermal Tests of Spherical Dome Protuberances on a at Flat Plate at a Mach Number of 6.5.," NASA Technical Paper 2631, 1986.

8. Glass, C. E., and R. L. Hunt, L.,. "Aerothermal Tests of Quilted Dome Models on a at Flat Plate at a Mach Number of 6.5.," NASA Technical Paper 2804, 1988.

9. Ostoich, C., D. J. Bodony, and P. H. Geubelle, ñDevelopment and validation of a first principles fluid-thermal multi-physics solver for hypersonic boundary layer heat transfer problems,ò AIAA 2011-1964, 2011.

10. Ostoich, C., D. J. Bodony, and P. H. Geubelle, ñFluid-Thermal Response of Spherical Dome Under a Mach 6.59 Laminar Boundary Layer,ò *AIAA Journal*, Vol. 50, No. 12, 2012.

11. Leyhe, E. W., and R. R. Howell, ñCalculation Procedure for Thermodynamic, Transport, and Flow Properties of the Combustion Products of a Hydrocarbon Fuel Mixture Burned in Air with Results for Ethylene-Air and Methane-Air Mixtures,ò NASA TN D-14, 1962.

12. Quiroz, R., J. Embler, R. Jacobs, G. Tzong, and S. Ligoure., ñPredictive Capability for Hypersonic Structural Response and Life Prediction: Phase II ï Detailed Design of Hypersonic Cruise Vehicle Hot-Structure,ò The Boeing Company Final Report, AFRL-RQ-WP-TR-2012-0265, 2012.

13. Zuchowski, B., H. Selby, J. Macguire, and P. McAuliffe, ñInvestigation of Shortfalls in Hypersonic Vehicle Structure Combined Environment Analysis Capability,ò AIAA-2011-2013, 2011.

14. Zuchowski, B., ñPredictive Capability for Hypersonic Structural Response and Life Prediction: Phase II ï Detailed Design of Hypersonic Cruise Vehicle Hot-Structure,ò Lockheed Martin Aeronautics Company Final Report, AFRL-RQ-WP-TR-2012-0280, 2012.